Int. J. Solids Structures, 1976, Vol. 12, pp. 67–79. Pergamon Press. Printed in Great Britain

STATIC AND DYNAMIC ANALYSIS OF THE DCB PROBLEM IN FRACTURE MECHANICS

M. SHMUELY and D. PERETZ

Department of Mechanics, Technion, Israel Institute of Technology, Haifa, Israel

(*Received* 18 *February* 1975; *revised* 12 *May* 1975)

Abstract—A finite difference scheme for treating the static and dynamic stress fields under plane-strain conditions in the DCB, is proposed. The adequacy of the scheme is established via the static solution by comparing the results obtained numerically with those obtained experimentally. Both the numerical and experimental results are also compared with data available in the literature. Discrepancies found are explained and discussed. For the numerical scheme adjusted to handle the propagating crack problem, the results represent a situation which is close to that observed experimentally; namely, an essentially constant steady state crack propagation speed from the start, with crack length at arrest and velocity values depending on the initial conditions. In addition, the velocities predicted by the analysis are shown to be in good agreement with those reported in the literature.

INTRODUCTION

The double cantilever beam (DCB) specimen (Fig. 1) is a well-established test configuration for studying both static and dynamic aspects of fracture mechanics. When first developed as a device for measuring fracture surface energies (or alternatively, stress intensity factors under plane strain conditions (K_{IC})) it was analysed by regarding the cracked portion of the specimen as a pair of built-in cantilever beams, employing the simple beam theory[1]. Later, a two-dimensional, linear elastic, numerical solution of the DCB static problem was proposed by Gross and Srawley[2]. In this solution the boundary collocation procedure was used to find the coefficients of the series terms in Williams stress function[3], by adjusting them to fit the boundary conditions imposed on the system, provided these conditions are defined in terms of tractions only. While the conditions along the free surfaces are well defined, there is some ambiguity in choosing the appropriate form of the traction distribution across the loading end which would properly represent the practical situation. The particular form of distribution assumed seems to have no appreciable effect on the K_I value determined from the last-mentioned analysis[4, 5]. This analysis was thus broadly accepted as a reliable method for characterising initial crack extension. Based on it is also the ASTM standard E399-70 T, in which a compact. DCB specimen is recommended for testing plane strain fracture toughness of metallic materials. Referring to the above-mentioned compact specimen, experiments show[4] that as far as displacements at the loading end are considered, results obtained from the boundary collocation analysis do not agree with the measured ones. This was attributed to the fact that the loading pins' holes are not well-approximated by the analysis.

In the dynamic case as yet only one-dimensional beam models have been employed. In order to take account of the region beyond the crack, Kanninen first proposed[6] a model which

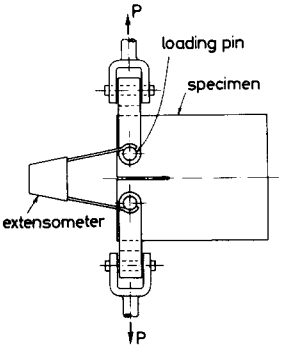

Fig. 1. Edge cracked plate specimen under loading.

consists of a simple Euler–Bernoulli beam lying on a Winkler elastic foundation. Later this model was modified to include lateral inertia ending with a Timoshenko beam lying on a more generalized elastic foundation[7].

The last mentioned model requires some information on the dynamic fracture toughness of the material in question. Calculations were performed with a crack speed independent dynamic toughness[7] and with crack speed dependent dynamic toughness values[8]. Results obtained were shown to be in good qualitative and quantitative agreement with the experimental results[9].

In this paper, a two-dimensional linear elastic numerical analysis of the DCB problem by a finite difference method is presented. Both the static and dynamic (with the time as an additional dimension) aspects of the problem are treated. Some experiments concerning the static situation were carried out. In order to establish the validity of the numerical scheme proposed, results obtained for the static problem are compared with the experimental measurements. A comparison is also made with data available in the literature. Subsequently, crack propagation under constant displacement conditions is simulated numerically for different initial stress intensity factors. The numerical results for the propagating crack, which is allowed to extend when the cleavage stress at a given distance from the crack tip reaches a predetermined level, describe a behavior close to that observed in experiments reported in the literature[9].

In the following sections, the elastic equations used are described. The appropriate finite difference scheme is constructed and examined. Experimental and numerical results for the static problem are presented and discussed. Preliminary results for the dynamic case are described.

2. ELASTIC EQUATIONS AND BOUNDARY CONDITIONS

The equations of motion in an elastic medium are

$$\rho\frac{\partial^2 U}{\partial t^2}=\frac{\partial\sigma_{xx}}{\partial x}+\frac{\partial\sigma_{xy}}{\partial y}$$
$$\rho\frac{\partial^2 V}{\partial t^2}=\frac{\partial\sigma_{xy}}{\partial x}+\frac{\partial\sigma_{yy}}{\partial y} \tag{1}$$

U and V are the displacements in the x and y direction respectively, ρ is the density and σ_{ij} the stress tensor.

The stress-strain relations are

$$\sigma_{xx}=(\lambda+2\mu)\frac{\partial U}{\partial x}+\lambda\frac{\partial V}{\partial y}$$
$$\sigma_{yy}=\lambda\frac{\partial U}{\partial x}+(\lambda+2\mu)\frac{\partial V}{\partial y} \tag{2}$$
$$\sigma_{xy}=\mu\left(\frac{\partial U}{\partial y}+\frac{\partial V}{\partial x}\right)$$

where λ and μ are Lamé constants, by which the dilatational and distortional velocities C_1 and C_2 are given

$$C_1^2=\frac{\lambda+2\mu}{\rho}$$
$$C_2^2=\frac{\mu}{\rho}. \tag{3}$$

Substituting (2) and (3) into (1), we obtain

$$\frac{\partial^2 U}{\partial t^2}=C_1^2\frac{\partial^2 U}{\partial x^2}+(C_1^2-C_2^2)\frac{\partial^2 V}{\partial x\partial y}+C_2^2\frac{\partial^2 U}{\partial y^2}$$
$$\frac{\partial^2 V}{\partial t^2}=C_2^2\frac{\partial^2 V}{\partial x^2}+(C_1^2-C_2^2)\frac{\partial^2 U}{\partial x\partial y}+C_1^2\frac{\partial^2 V}{\partial y^2}. \tag{4}$$

The wave eqns (4) govern the dynamic state of the elastic system under consideration. The static solution, in which we are also interested, can be obtained by solving the time-independent version of eqns (4), namely, a set of elliptic partial differential equations customarily solved numerically by interative processes. However, by employing the dynamic relaxation method [10, 11], essentially the same numerical scheme is used for solving both the dynamic and static problems. According to this method, eqns (4) are modified to

$$\theta\frac{\partial U}{\partial t}+\frac{\partial^2 U}{\partial t^2}C_1^2\frac{\partial^2 U}{\partial x^2}+(C_1^2-C_2^2)\frac{\partial^2 V}{\partial x\partial y}+C_2^2\frac{\partial^2 U}{\partial y^2}$$

$$\theta\frac{\partial V}{\partial t}+\frac{\partial^2 V}{\partial t^2}=C_2^2\frac{\partial^2 V}{\partial x^2}+(C_1^2-C_2^2)\frac{\partial^2 U}{\partial x\partial y}+C_1^2\frac{\partial^2 V}{\partial y^2} \tag{5}$$

In eqns (5), by letting θ be equal to zero, we obviously return to wave eqns (4), whereas if $\theta>0$, successive changes in displacements, occurring in real time, correspond to successive numerical two-point semi-iterative cycles, converging finally to the static solution. A numerical scheme related to eqns (5) is thus easily adjusted to treat either the static problem or the dynamic problem, just by substituting the appropriate value for θ. This enables, as will be demonstrated later, the construction of a compact and relatively simple computer program to simulate the fracture process in the DCB, including both fracture initiation (the static problem) and crack extension (the dynamic problem). Moreover, the validity of the complete numerical scheme may be verified by referring to results drawn from either the static solution or the dynamic solution.

A solution of eqns (5) corresponding to a symmetrically loaded specimen (see Fig. 2) is symmetric with respect to the x axis. It is thus sufficient to consider the upper part of the specimen ($y\geq 0$), provided that the boundary conditions related to that part are supplemented by the symmetry conditions along the segment ($y=0$; $a<x\leq L$). Referring to the upper part and considering a fixed grips case, the following conditions should be satisfied:

$$\begin{aligned}
&\sigma_{yy}=0;\quad \sigma_{xy}=0 \quad \text{on} \quad y=0 \quad \text{for} \quad 0\leq x<a\\
&V=0;\quad \sigma_{xy}=0 \quad \text{on} \quad y=0 \quad \text{for} \quad a<x\leq L\\
&\sigma_{xx}=0;\quad \sigma_{xy}=0 \quad \text{on} \quad x=0, L \quad \text{for} \quad 0\leq y\leq H\\
&\sigma_{yy}=0;\quad \sigma_{xy}=0 \quad \text{on} \quad y=H \quad \text{for} \quad 0\leq x\leq L\\
&V(x_0, y_0)=D \quad \text{for all } t,
\end{aligned} \tag{6}$$

where D is the constant deflection value of the point (x_0, y_0) at which the load is provided, and a is the crack length.

By using the constitutive eqns (2), those conditions (6) which involve stresses are expressed in terms of displacements and their derivatives, so that both conditions (6) and the differential eqns (5) are then related to the same unknowns.

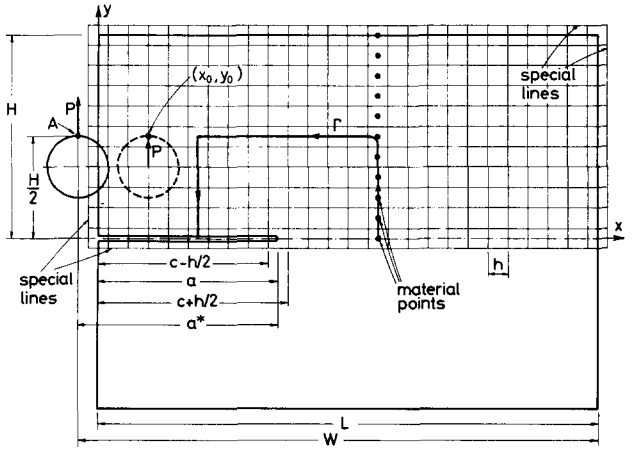

Fig. 2. Scheme of grid used.

3. FINITE DIFFERENCE SCHEME

Equations (5) subject to conditions (6) are solved by a method of finite differences, similar to that used by Shmuely and Alterman[12] to analyse crack propagation in infinite plates.

A grid is imposed on the upper half of the specimen, Fig. 2. For convenience, the mesh size h is taken to be the same in both the x and y directions, The value of h is such that both the length L and the height H of the specimens are integer multiples of h. The grid is extended beyond the half specimen by adding the four special grid lines $x = -h/2$, $x = L + h/2$, $y = -h/2$ and $y = H + h/2$ which form the grid boundaries.

Denoting the time increment by k and using central difference approximations, the finite difference formulation of equations (5), valid at the inner part of the grid, is

$$\begin{aligned} U(x, y, t+k) = {} & 1/(1+0{\cdot}5k\theta)\{2U(x, y, t) - (1-0{\cdot}5k\theta)U(x, y, t-k) \\ & + (C_1 k/h)^2[U(x+h, y, t) - 2U(x, y, t) + U(x-h, y, t)] \\ & + (C_1^2 - C_2^2)(k/2h)^2[V(x+h, y+h, t) - V(x+h, y-h, t) \\ & - V(x-h, y+h, t) + V(x-h, y-h, t)] \\ & + (C_2 k/h)^2[U(x, y+h, t) - 2U(x, y, t) + U(x, y-h, t)]\} \end{aligned} \tag{7}$$

$$\begin{aligned} V(x, y, t+k) = {} & 1/(1+0{\cdot}5k\theta)\{2V(x, y, t) - (1-0{\cdot}5k)V(x, y, t-k) \\ & + (C_2 k/h)^2[V(x+h, y, t) - 2V(x, y, t) + V(x-h, y, t)] \\ & + (C_1^2 - C_2^2)(k/2h)^2[U(x+h, y+h, t) - U(x+h, y-h, t) \\ & - U(x-h, y+h, t) + U(x-h, y-h, t)] \\ & + (C_1 k/h)^2[V(x, y+h, t) - 2V(x, y, t) + V(x, y-h, t)]\}. \end{aligned}$$

The displacements at mesh points lying on the special lines are determined by satisfying the boundary conditions. By approximating the conditions $\sigma_{xx} = \sigma_{xy} = 0$ on $x = 0$ and $x = L$, we obtain respectively for points on the grid lines $x = -h/2$ and $x = L + h/2$

$$U\left(\begin{matrix}-h/2\\ L+h/2\end{matrix}, y, t\right) = U\left(\begin{matrix}h/2\\ L-h/2\end{matrix}, y, t\right) \pm \left(\frac{C_1^2 - 2C_2^2}{2C_1^2}\right)\left[V\left(\begin{matrix}h/2\\ L-h/2\end{matrix}, y+h, t\right) - V\left(\begin{matrix}h/2\\ L-h/2\end{matrix}, y-h, t\right)\right]$$

$$V\left(\begin{matrix}-h/2\\ L+h/2\end{matrix}, y, t\right) = V\left(\begin{matrix}h/2\\ L-h/2\end{matrix}, y, t\right) \pm 0{\cdot}5\left[U\left(\begin{matrix}h/2\\ L-h/2\end{matrix}, y+h, t\right) - U\left(\begin{matrix}h/2\\ L-h/2\end{matrix}, y-h, t\right)\right]. \tag{8}$$

On the grid lines $y = -h/2$ and $y = H + h/2$, we obtain

$$U\left(x, \begin{matrix}-h/2\\ H+h/2\end{matrix}, t\right) = U\left(x, \begin{matrix}h/2\\ H-h/2\end{matrix}, t\right) \pm 0{\cdot}5\left[V\left(x+h, \begin{matrix}h/2\\ H-h/2\end{matrix}, t\right) - V\left(x-h, \begin{matrix}h/2\\ H-h/2\end{matrix}, t\right)\right]$$

$$\begin{aligned} V\left(x, \begin{matrix}-h/2\\ H+h/2\end{matrix}, t\right) = {} & V\left(x, \begin{matrix}h/2\\ H-h/2\end{matrix}, t\right) \pm \left(\frac{C_1^2 - 2C_2^2}{2C_1^2}\right)\left[U\left(x+h, \begin{matrix}h/2\\ H-h/2\end{matrix}, t\right)\right. \\ & \left. - U\left(x-h, \begin{matrix}h/2\\ H-h/2\end{matrix}, t\right)\right] \end{aligned} \tag{9}$$

where the last equation as related to $y = -h/2$ is valid only along the crack surface, namely, only for $x \leqslant c - (h/2)$, with c denoting the distance from the y-axis to the midpoint of that grid interval, on $y = 0$, in which the crack terminates.

From conditions (6), on $y = 0$ and ahead of the crack, $V = 0$. To satisfy this condition the V displacement on $y = -h/2$ is approximated by

$$V(x, -h/2, t) = -V(x, h/2, t) \quad \text{for} \quad x \geqslant c + h/2. \tag{10}$$

In constructing the approximations (8) and (9) we follow a method proposed by Alterman and Rotenberg[13] which was also successfully employed in [12] and [14]. According to this method,

derivatives perpendicular to the boundary are approximated by uncentered differences and derivatives parallel to the boundary by centered differences. The real boundaries can then be considered as located at a distance of half the mesh size from the grid boundaries (see Fig. 2).

From (10) and the relevant part of [9], it follows that the crack tip is confined to lie on the open interval $c - h/2 < x < c + h/2$. As will become obvious later, any assumption concerning the exact location of the crack tip has no bearing on results or conclusions drawn from the numerical solution. The only occasion where it may have any significance is when comparing numerical and experimental results. In this case, however, it is the complete crack length which counts, so that any error introduced in locating the crack tip should be related to the full crack length. In [12] it was shown that the crack tip may be approximately assumed as being located in the middle of the above mentioned interval. By adhering to this assumption (which means that the value of c may be identified with the crack length a) the error introduced in estimating the crack length cannot exceed $h/2$. If, in addition, we refine the grid, the relative error can be reduced to at least the same degree as the expected experimental errors.

The four grid corners require a special treatment. Different methods of handling the discontinuities at such points have been proposed in the past[13, 14]. Here we found that satisfactory results are obtained when the displacements sought are extrapolated from those given along both sides of the corner in question. Accordingly, the U and V components at $(-h/2, -h/2)$ are given by

$$\begin{matrix} U \\ V \end{matrix}(-h/2, -h/2, t) = \begin{matrix} U \\ V \end{matrix}(h/2, -h/2, t) + \begin{matrix} U \\ V \end{matrix}(-h/2, h/2, t) - 0{\cdot}5\left[\begin{matrix} U \\ V \end{matrix}(3h/2, -h/2, t) + \begin{matrix} U \\ V \end{matrix}(-h/2, 3h/2, t)\right]. \tag{11}$$

Similar expressions are used for deriving the displacement components at $(-h/2, H + h/2)$, $(L + h/2, H + h/2)$ and $(L + h/2, -h/2)$.

The method of prescribing the constant deflection D in the scheme needs some explanation. If the deflection is prescribed at some point inside the grid, the loaded point should be part of a boundary formed by cutting out a hole in the grid, so that a multiply connected region is obtained (see Fig. 2). To obtain a stable scheme the cutout should be sufficiently large. To keep the correct proportions of the specimen, this would imply an extension of the grid requiring a larger memory and consuming more computer time.

It is much more efficient to assign the constant deflection to a point on the boundaries of the original simple connected region even if it is intended to simulate a practical situation in which the deflection is prescribed at some point inside the specimen at a distance of, say, $y = y_0 < H$ from the crack surface. In this case the point $(0, y_0)$ is displaced vertically to a distance D by approximating the V-displacement of the respective grid point $(-h/2, y_0)$ by

$$V(-h/2, y_0, t) = 2D - V(h/2, y_0, t) \quad \text{for all } t \tag{12}$$

which overrides the displacement obtained previously at the same point in eqn (8). It will be shown later that by so doing it is possible to define uniquely the location and the value of a concentrated force which when applied to the specimen in question would yield a stress field similar to the one obtained numerically.

The resulting stresses and displacements, as referred to in the subsequent discussion, are related to points located at the middle of the mesh openings. These points will be designated hereafter as material points, to distinguish them from the grid points used in deriving the solution. Some material points are shown in Fig. 2.

In all cases described hereafter, the scheme was run with a dilatational wave velocity $C_1 = 1$, a specimen height of $H = 1$, and a material density of $\rho = 1$. The particular material investigated is distinguished, in the scheme, by its Poisson ratio ν which determines the distortional wave velocity

$$C_2 = C_1\left[\frac{1-2\nu}{2(1-\nu)}\right]^{1/2}. \tag{13}$$

It is the ratio $(C_1/C_2)^2 = 2(1-\nu)/(1-2\nu)$ that determines the upper bound for the ratio of the time step to the space step $\alpha = k/h$, with which the two-dimensional finite difference scheme is still stable. An elementary stability analysis[15] shows that for $\nu = 0{\cdot}25$ α should be less than 0·86 but might be greater if ν is increased. To be on the safe side, we choose in all cases $\alpha = 0{\cdot}8$.

All calculations were performed on an IBM 370/168 computer. About one minute computation time was needed for 600 time steps with a grid of about 1500 mesh points.

4. ACCURACY OF THE FINITE DIFFERENCE CALCULATION

The accuracy of the numerical scheme is checked via the static solution. As mentioned above, the numerical solution converges to the static solution if θ (see eqns 5 and 7) is different from zero and positive. After some trials, it was found that the fastest convergency is achieved with θ of about $0{\cdot}05/h$.

Given θ, we seek the largest possible mesh size for which results derived are still sufficiently accurate. To this end, calculations are repeated for the same specimen with different mesh sizes. Results were drawn for a specimen geometry of $H/a/L = 1/1/3$, with the space increment h taking, in turn, the values $H/10$, $H/15$, $H/20$, $H/25$ and $H/28$. The Poisson ratio chosen was $\nu = 0{\cdot}395$. This value corresponds to the sort of perspex from which specimens used in the experiments, described later, were made. In all cases, the specimen is subjected to a constant deflection $D = H$ at the point $(0, H/2)$, which is introduced in the scheme by the approximation (12).

Every 100 time steps (i.e. iterations) the grid is scanned to find

$$s = \max\left(|U(x, y, t+k) - U(x, y, t)| + |V(x, y, t+k) - V(x, y, t)|\right); \quad 0 \leq x \leq L, \quad 0 \leq y \leq H. \tag{14}$$

Note that s is one of the possible measures for convergency of the solution. Beginning with the 400th time step, we calculate and record in addition the following variables:

(1) The value

$$E_k = \frac{1}{2}\rho \int_0^L \int_0^H \left[\left(\frac{\partial U}{\partial t}\right)^2 + \left(\frac{\partial V}{\partial t}\right)^2\right] \mathrm{d}x\, \mathrm{d}y \tag{15}$$

which in the dynamic case equals the total kinetic energy but in the static case serves as an additional indicator of the solution's convergency.

(2) The total potential energy E_p

$$E_p = \int_0^L \int_0^H \frac{1}{2E}[(1-\nu^2)(\sigma_{xx}^2 + \sigma_{yy}^2) + 2(1+\nu)(\sigma_{xy}^2 - \nu\sigma_{xx}\sigma_{yy})]\, \mathrm{d}x\, \mathrm{d}y \tag{16}$$

with E standing for Young's modulus.

(3) The shear forces along the x axis for $0 < x < a$

$$Q(x) = \int_0^H \sigma_{xy}(x, y)\, \mathrm{d}y. \tag{17}$$

(4) The axial forces on cross sections perpendicular to the x axis

$$F(x) = \int_0^H \sigma_{xx}(x, y)\, \mathrm{d}y \quad \text{for} \quad 0 < x < a. \tag{18}$$

(5) The strain-energy release rate which is evaluated by a method proposed by Rice[16]. It was shown[17] that the path-independent integral

$$J = \int_\Gamma \left(W\, \mathrm{d}y - \mathbf{T}_r \frac{\partial \mathbf{U}}{\partial x}\, \mathrm{d}s\right) \tag{19}$$

gives the desired strain-energy-release rate. Γ is a curve surrounding the crack tip, W is the strain energy density, $\mathbf{T}_r$ is the traction vector and $\mathbf{U}$ is the displacement vector. Due to symmetry it suffices here to calculate the integral along a curve which lies only above the x-axis. The path used is depicted in Fig. 2.

(6) The stress intensity factor K_I, which is obtained from J by

$$K_I = \left(\frac{EJ}{1-\nu^2}\right) \quad \text{for plain strain.} \tag{20}$$

By employing the path-independent integral (19) in deriving K_I we avoid referring to the detailed configuration of stresses in the close neighborhood of the crack tip which would have implied a relatively dense grid.

The integrations in (15)–(19) are performed by Simpson's rule, employing the subroutine *QSF*, as provided by IBM[18]. The corresponding integrands are related to material points.

It was found that values of s/H or $E_k/C_1^2\rho H^2$ of the order of 10^{-4} or 10^{-7} respectively indicate that the final solution has been reached, since further iterations give changes in values of E_p or J which are less than 0·1% per 100 iterations. With mesh sizes smaller than $H/20$ values of E_p, J or K differ by less than 1% from those obtained with $h = H/20$. This confirms the validity of the approximation used here and shows that there is no advantage in mesh sizes smaller than $H/20$.

The imposed boundary conditions imply a constant shear force Q and a zero axial force F along the crack arm. The calculated Q and F show only slight discrepancies from this situation (see Fig. 6b). These discrepancies decrease with decreasing mesh size. The average of Q along the crack arm is denoted hereafter as P. Differences in P due to changes in mesh size were found to be less than 1%.

With P considered as a concentrated force which when applied to the specimen would yield a stress field similar to the one obtained numerically, the work done by this force should be equal to the strain energy E_p. Hence the deflection δ at the point of the force application is given by $\delta = 2E_p/P$. Recall that in the scheme, the vertical displacement D was prescribed to the point $(0, H/2)$, in such a way that the cross section $x = 0$ is disturbed at a height $H/2$ above the crack, but is otherwise stress-free. The force P may thus be envisioned as applied in the neighborhood of $(0, H/2)$, at a point along $y = H/2$, the vertical displacement of which is δ, provided it is found to lie not too far from $x = 0$. Given the V displacement component at the material points $(0, H/2)$ and $(h, H/2)$, the force point of application is found by a linear interpolation if $\delta < D$ or by a linear extrapolation if $\delta > D$. The horizontal distance from the force point of application to the crack end, denoted hereafter by a^*, is practically the distance from the vertical center line of the loading pin to the crack end, referred to in the literature as the crack length. Given a^*, the distance from P to the free end of the specimen is then $W = a^* - a + L$ (see Fig. 2). By employing the just-described technique of determining the dimensions of the specimen simulated by the numerical scheme, we avoid working with the "multiply-connected region" problem.

5. SOME NUMERICAL AND EXPERIMENTAL RESULTS FOR THE STATIC CASE

Three classes of specimens were investigated. They are distinguished by their respective geometry and material constants. In the first class, A, we treat relatively long specimens ($W/H = 3{\cdot}06$) with the objective of analysing geometries such as those which appear in the dynamic problems of crack propagation and arrest[6, 7, 9]. The specimen geometry in the second and third classes, B and C, is the one specified in ASTM Standard E 399-70 T (i.e. $W/H = 1{\cdot}667$ and $a^*/W \sim 0{\cdot}45$–$0{\cdot}55$) known also as the compact specimen, for which detailed results are available in the literature[4], obtained so far, numerically, by the collocation method. In each class, keeping W/H constant, the scheme was run with a variety of crack lengths. In class A and B the analysis was carried out with a Poisson ratio of $\nu = 0{\cdot}395$, corresponding to the Poisson ratio of PMMA from which the experimental samples were made. In class C we change ν to 0·3 in order to learn the effect of the material constants on the results, simulating in this case specimens of steel.

The adequacy of the elastic solution proposed here was established by comparing the stiffness δ/P as predicted by the numerical analysis with that obtained experimentally. To this end

specimens cut out from 10 mm sheets of PMMA were machined to size and tested on an Instron machine. The class A specimens ($W/H = 3{\cdot}06$) were 90 mm long with $W = 85{\cdot}5$ mm and a pin diameter of 6 mm. The ratio between the pin diameter and the specimen height H, denoted hereafter as β, was, thus $\beta = 0{\cdot}215$. Two sorts of class B specimens ($W/H = 1{\cdot}667$) were tested. The first 130 mm long with $W = 120$ and a pin diameter of 6 mm so that β is reduced to 0·083; the second 75 mm long with $W = 60$ and the pin, as specified by the ASTM Standard, $0{\cdot}25W = 15$ mm in diameter so that $\beta = 0{\cdot}417$. Special grips were constructed to ensure perfect alignment and pure tension. The loading pins were separated at a constant rate of 0·2 mm/min. The load, measured by a load cell, and the deflection, measured by an extensometer (see Fig. 1) were continuously recorded. For the relatively low loading levels applied, the PMMA showed a linear behavior. From the slope of the curve recorded, the stiffness of δ/P was determined. Experimental results for class A and the two kinds of class B specimens are shown in Figs. 3 and 4 respectively. In these figures, the numerical non-dimensional results were divided by $C_1^2\rho = 622{\cdot}3\ \text{kg/mm}^2$ which corresponds to $E = 301\ \text{kg/mm}^2$ and $\nu = 0{\cdot}395$, which were the material properties found experimentally for PMMA. From the excellent matching of experimental and calculated results when $\beta = 0{\cdot}083$, compared with the slight discrepancies encountered with $\beta = 0{\cdot}215$ (for $W/H = 3{\cdot}06$), and the greater discrepancies in case $\beta = 0{\cdot}417$, recalling, in addition, that in the scheme, the disturbances caused by the load were restricted to one mesh point, we may infer that the finite difference solution provides us with an accurate picture of the static stress-strain field in the DCB, as long as the loading pin diameter is small compared with the other dimensions of the specimen. If necessary, the scheme can be modified to account also for larger pin diameters by solving the multiply-connected region problem as previously mentioned.

From the fracture mechanics point of view, however, the fact that displacements are correctly predicted by the scheme, although encouraging, is still not sufficient. The new proposed method should be tested against its capability of predicting the correct stress intensity factor, as well. This is done by comparing the stress intensity factors K_I as derived from the present solution (eqn 20) with established values from the literature (Table 1). For each case listed in Table 1, we evaluate and record the dimensionless coefficients: $N_1 = K_I H^{3/2}/Pa^*$ as suggested in [2],

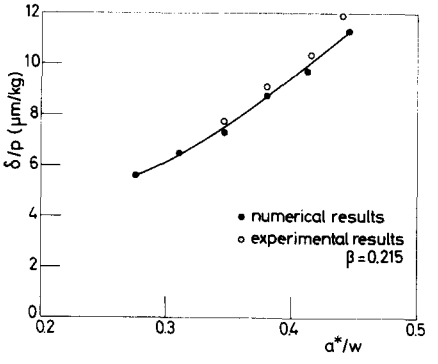

Fig. 3. Relation between stiffness and crack length for case A specimens ($W/H = 3{\cdot}06$; $\nu = 0{\cdot}395$).

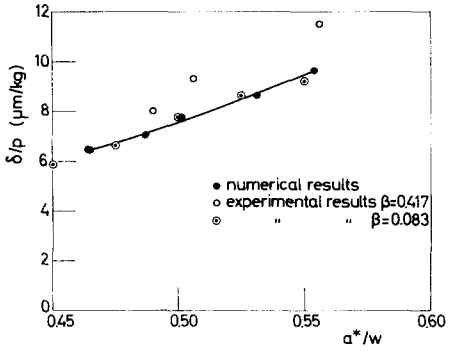

Fig. 4. Relation between stiffness and crack length for case B specimens (compact specimen; $\nu = 0{\cdot}395$).

Table 1.

Serial No.	Specimen charac. Class	a^*/W	$K_I/C_1^2\pi H_2^{\frac{1}{2}}$	$N_1=\frac{K_I H^{\frac{1}{2}}}{Pa^{*\frac{1}{2}}}$	$N_2=\frac{K_I(W-a^*)^{\frac{3}{2}}}{P(2W+a^*)}$	$N_3=\frac{K_I W^{\frac{1}{2}}}{P}$	R_2	R_3
1	A	0.275	0.1681	5.9606	2.3735	8.7454	1.039	
2	W/H=3.06	0.310	0.1508	5.5971	2.2978	9.2619	1.026	not
3	ν=0.395	0.346	0.1356	5.1765	2.1620	9.6028	1.001	avail-
4		0.380	0.1232	5.1270	2.1330	10.4060	0.979	able
5	(PMMA)	0.412	0.1115	4.7838	1.9747	10.5745	0.982	
6		0.446	0.1016	4.6451	1.8761	11.1161	0.978	
7		0.465	0.2057	8.9976	1.4316	9.0132	1.035	1.041
8	B	0.487	0.2008	9.1976	1.4291	9.6708	1.042	1.046
9	W/H=1.666	0.509	0.1959	9.4722	1.4304	10.4278	1.051	1.057
10	ν=0.395	0.531	0.1911	9.8076	1.4339	11.3160	1.060	1.069
11	(PMMA)	0.554	0.1864	10.2442	1.4431	12.3677	1.074	1.084
12		0.443	0.2997	9.0010	1.4601	8.5871	1.046	1.049
13	C	0.464	0.2914	9.1422	1.4528	9.1266	1.050	1.054
14	W/H=1.666	0.486	0.2833	9.3097	1.4474	9.7521	1.053	1.058
15	ν=0.3	0.508	0.2755	9.5649	1.4413	10.4587	1.059	1.065
16	(steel)	0.530	0.2680	9.8541	1.4373	11.2769	1.063	1.071
17		0.551	0.2602	10.2332	1.4360	12.1823	1.068	1.078

$N_2 = K_I(W - a^*)^{3/2}/P(2W + a^*)$ as suggested in [4], and $N_3 = K_I W^{1/2}/P$ given in ASTM Standard as a function of a^*/W. The ratio R_2 between N_2 and the value obtained by interpolating (or extrapolating, if necessary) the data given in [4, Table 3], and the ratio R_3 between N_3 and the corresponding coefficient provided by the ASTM Standard ($f(a^*/W)$ there) are respectively recorded in column 7 and column 8 of Table 1.

In the values of both R_2 and R_3, results drawn from the present analysis are compared with results derived by the boundary collocation analysis [2, 4] which to the best of our knowledge is the most elaborate method used so far for handling the DCB crack initiation problem. The two approaches just mentioned differ by the kind of boundary value problem solved by them. Note that in the present analysis a mixed boundary value problem was solved, since a displacement condition at one of the boundary points was satisfied with the remaining boundary left traction free. At least for relatively small loading pins it was shown to be an appropriate way of handling the DCB problem. The collocation procedure, however, applied in conjunction with Williams' stress function (or, alternatively, with Airy stress function [19]) is confined to cases where, on the boundary, only tractions are prescribed (known also as the first fundamental boundary value problem in elasticity [20]). Thus, to tackle the DCB problem by the last-mentioned method, some kind of assumption should be made as to the stress distribution along (or nearby [2]) the resultant force line of action. The distribution of shear and normal stresses along some cross sections of the compact specimen crack arm (cases 10 and 14 of Table 1) as obtained from the present analysis, are depicted in Figs. 5 and 6. The distribution near the resultant force is seen to be quite different from the parabolic distribution of shear stresses assumed by Srawley and Gross [4] or the linear one assumed by Wiederhorn *et al.* [5]. Nevertheless, as demonstrated by the values of R_2 and R_3 in Table 1, the K_I values predicted by the finite difference analysis are very close to those obtained by the boundary collocation analysis. It seems that the affect of the specific condition prescribed at the loaded end of the specimen, on the K_I value is small. Practically, it means that experimental measurements of K_{IC} would hardly help in deciding upon which of the numerical methods is more accurate. Nevertheless, we may conclude that the finite difference method suggested here is well adapted for handling the DCB fracture problem.

6. PRELIMINARY RESULTS FOR THE DYNAMIC CASE

Encouraged by the satisfactory results obtained from the finite difference analysis in the static case and recalling that essentially the same scheme, with one minor change (reducing θ to zero)

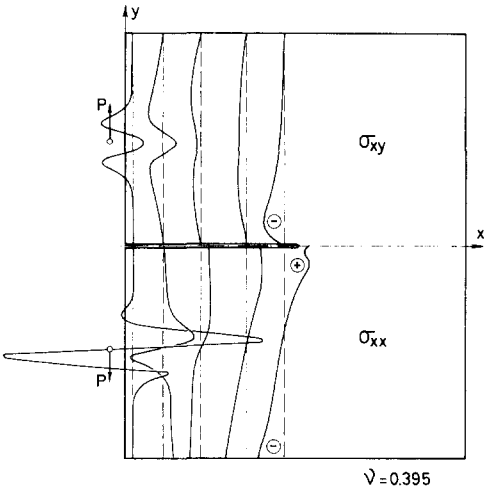

Fig. 5. Shear and normal stress distributions in the DCB.

may control a dynamic situation, we proceed towards examining the crack propagation problem. To decide upon which of the two possible fracture criteria (i.e. stress or energy) is the appropriate one, we may, as suggested in [8], axiomatically accept each of them and check the consequences. Preliminary results obtained here from the two dimensional dynamic solution seem to favor the stress criterion.

The simulation of a fracturing process in a DCB runs as follows. Given the specimen geometry and its material constants we first solve the static problem in the way previously described. The solution is assumed to approximate the static state when s (as defined in (14)) is less than $0{\cdot}25\ 10^{-4}$. At this stage the σ_{yy} stress level at $(c + h/2, 0)$, denoted hereafter as σ_q, is recorded, θ is reduced to zero and the crack is extended by one grid interval. In the following time steps the boundary conditions related to the crack length, eqns (9) and (10), are applied while taking into account the fact that c was enlarged by one grid interval. The other boundary conditions, including the constant displacement at $(0, H/2)$, remain unchanged. As a result of the above described changes, a dynamic state of stress is built up in the specimen. In particular the σ_{yy} stress level at $(c + h/2, 0)$ begins to rise. When this stress level reaches a prescribed critical

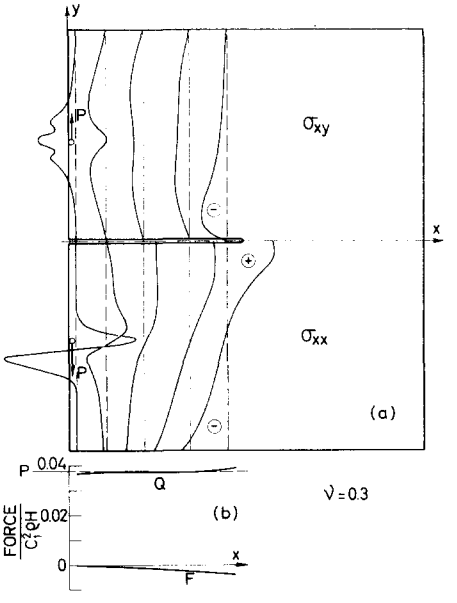

Fig. 6. Shear stresses, normal stresses and force distribution in the DCB.

value σ_c, the crack is further extended by one grid interval. The crack now continues to grow, by one grid interval at a time, as long as the σ_{yy} stress level ahead of the propagating crack tip reaches the value of σ_c. The crack is assumed to be arrested, when a relatively long time passes, after the last extension, with the σ_{yy} stress level, ahead of its tip, remaining below the critical value σ_c. During the propagation stage the time that elaspses between two sequential extensions is recorded and the corresponding velocity is evaluated.

The above described procedure was conducted, keeping the same geometry and material constants, with various values of σ_c, which is chosen to be either equal to or less than σ_q. Note that by changing the ratio σ_q/σ_c we actually change the conditions under which the fracture is initiated. In fact, a $\sigma_q > \sigma_c$ indicates that the stress intensity factor (K_q) at initiation is higher than K_{IC}. Such a situation is in practice encountered with a blunted crack tip.

Some results are described in Figs. 7 and 8. The results are related to a specimen which was tested by Hahn *et al.* as described on page 9 of [9]. (The pin diameter in the specimen mentioned was $\beta \simeq 0{\cdot}40$ time the height H). In the numerical scheme the relations $a^*/H/W$ were accordingly chosen to be $1{\cdot}075/1/4{\cdot}4$ and $\nu = 0{\cdot}3$. When interpreting the results it should be remembered that at each time step, stresses undergo finite changes, therefore, when crack extension occurs, the stresses at the point $(c + h/2, 0)$ almost always exceed the critical stress value σ_c (in each extension by a different amount). Moreover, the time that passes between two extensions is an integral multiple of the time increment k, so that for each value of $\alpha = k/h$ the numerical scheme may yield only discrete values of velocities. Nevertheless, results were remarkably insensitive to the choice of α.

Starting with $\sigma_q/\sigma_c = 1$ and increasing this ratio by $0{\cdot}125$ at a time, eleven different fracture initiation conditions were investigated, the last of which corresponds to $\sigma_q/\sigma_c = 2{\cdot}25$. For $\sigma_q/\sigma_c = 1$ we found that the crack, although initially extended by one grid interval, does not continue to grow. In all other cases the crack propagates for a while and then stops. The extension of the crack in the course of time for two values of σ_q/σ_c is given in Fig. 7 which shows that while crack propagation does not occur at a precisely constant velocity, the crack-length-time plots are close to being linear. This happens in the other cases as well. The velocity

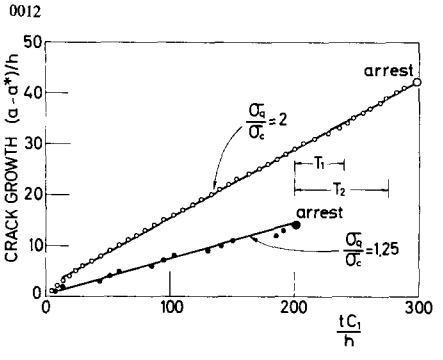

Fig. 7. Assorted crack length time data for two initiation conditions.

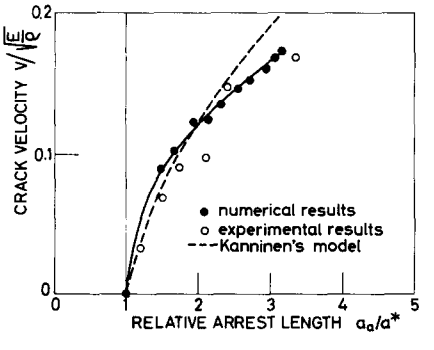

Fig. 8. Relation between crack velocity and crack growth.

fluctuations, which are remarkable for small value of σ_q/σ_c and diminish when this ratio increases, may be attributed to the stress waves which return from the free boundaries. For reference, the time intervals T_1 and T_2 required for dilatational and distortional waves respectively to travel from the crack plane to the lateral surface and return, are also shown in Fig. 7. Reasonable correlation obtained between the time intervals mentioned and the intervals elapsing between successive points indicating velocity changes. Notice also that the crack length at arrest a_a and the crack speed increase with σ_q/σ_c. When all cases are considered it is found that both a_a and the crack speed are single valued monotonically increasing functions of σ_q/σ_c.

Perhaps the most important findings of the present research are the agreements between the predictions of the finite difference analysis and the experimental observations reported by Hahn *et al.*[9]. According to the last authors, crack propagation and arrest in the DCB specimen can be characterized by the following: "(1) The crack propagates at an essentially constant steady-state velocity from the start. (2) The steady state velocity is not an invariant but depends on the initial conditions, i.e. the bluntness of the starting slot. (3) For a given DCB configuration, material density and modulus, the crack velocity and arrest length are separate single value functions of R or K_d." R and K_d are respectively defined as "the dynamic fracture energy and fracture toughness of a fast running crack." Here, however, the notion of K_d is replaced by the critical stress criterion σ_c. It was further noticed that the present analysis succeeds in approximating the experimental measurements quantitatively as well.

In Fig. 8 we compare the numerical results derived here with experimental measurements reported in [9] of the relation between crack velocity and crack length at arrest. By the numerically calculated crack velocity in this figure, we mean the average of the velocities encountered during the propagation. This average might deviate from the velocity obtained by drawing a straight line through the points appearing in the crack length-time plots, particularly for smaller ratios of σ_q/σ_c. In Fig. 8 we show also the curve obtained from the one dimensional Timoshenko beam model proposed by Kanninen[9]. This model has also been shown[7, 8] to predict the same kind of behaviour of the propagating crack in the DCB as was previously described.

Acknowledgements—The authors wish to express their thanks to Dr. M. F. Kanninen for interesting them in the problem and providing them with the results of experiments carried out in Battelle, Ohio. This research is partially supported by funds of the Technion and partially by the Mechanics Research Center at the Department of Mechanics, Technion–Israel Institute of Technology, Haifa.

REFERENCES

1. J. J. Gilman, Cleavage, ductility and tenacity in crystals. In *Fracture* (Edited by B. L. Averbach *et al.*), p. 193. The Technology Press of M.I.T. (1959).
2. B. Gross and J. E. Srawley, *Stress Intensity Factors by Boundary Collocation for Single-Edge-Notch Specimens Subject to Splitting Forces.* NASA TND-3295 (1966).
3. M. L. Williams, On the stress distribution at the base of a stationary crack, *J. Appl. Mech.* **24**, 109 (1957).
4. J. E. Srawley and B. Gross, Stress intensity factors for bend and compact specimens. *Eng. Fracture Mech.* **4**, 587 (1972).
5. S. M. Wiederhorn, A. M. Shorb and R. L. Moses, Critical analysis of the theory of the double cantilever method of measuring fracture-surface energies. *J. Appl. Phys.* **39**, 1569 (1968).
6. M. F. Kanninen, An augmented double cantilever beam model for studying crack propagation and arrest. *Int. J. Fracture* **9**, 83 (1973).
7. M. F. Kanninen, A dynamic analysis of unstable crack propagation and arrest in the DCB test specimen. *Int. J. Fracture* **10**, 415 (1974).
8. M. F. Kanninen, An analysis of dynamic crack propagation and arrest for a material having a crack speed dependent fracture toughness, In *Prospects of Fracture Mechanics* (Edited by G. C. Sih *et al.*). Noordhoff, Leyden, The Netherlands (1974).
9. G. T. Hahn, R. G. Hoagland, M. F. Kanninen, A. R. Rosenfield and R. Sejnoha, Fast fracture resistance and crack arrest in structural steels. SSC-242 Progress Report on Project SR-201, pp. 1–24. Dept. of the Navy (1973).
10. A. S. Day, *An Introduction to Dynamic Relaxation.* The Engineer, London (1965).
11. W. R. Hodgkins, On the relation between dynamic relaxation and semi-iterative matrix methods. *Numerische Mathematik* **9**, 446 (1967).
12. M. Shmuely and Z. S. Alterman, Crack Propagation Analysis by Finite Difference, *J. Appl. Mech.* **40**, 902 (1973).
13. Z. S. Alterman and A. Rotenberg, Seismic waves in a quarter plane, *Bull. Seism. Soc. Am.* **59**, 347 (1969).
14. Z. S. Alterman and D. Loewenthal, Seismic waves in a quarter and three quarter plane. *Geophys. J., Roy. Astr. Soc.* **20**, 101 (1970).
15. M. Shmuely, A three dimensional numerical analysis of stress distribution in the vicinity of a crack tip. *Israel J. Tech.* **9**, 523 (1971).
16. J. R. Rice, Mathematical analysis in the mechanics of fracture. In *Fracture*, Vol. 2, (Edited by H. Liebowitz). Academic Press, New York (1968).

17. J. R. Rice, A path independent integral and the approximate analysis of strain concentration by notches and cracks, *J. Appl. Mech.* **35**, 379 (1968).
18. I.B.M., System/360 Scientific Subroutine Package, Publication No. H20-0205-3.
19. W. K. Wilson, Numerical methods for determining stress intensity factors of an interior crack in a finite plane, *J. Basic Eng.* **93**, 685 (1971).
20. I. S. Sokolnikoff, *Mathematical theory of Elasticity*, 2nd Edn, p. 73. McGraw-Hill, New York (1956).